An Adaptive Variable-Frequency Control With Constant Crossover Frequency Achieving Fast Transient Response for Wide-Operation-Range Flyback Converter

Ching-Hsiang Cheng, *Student Member, IEEE*, Ching-Jan Chen, *Senior Member, IEEE*, and Shinn-Shyong Wang

***Abstract*—Flyback converters with universal serial bus power delivery (USB-PD) specification are widely used in low-power adapter application. The wide output voltage range operation of USB-PD makes the loop gain vary under different working conditions. To ensure stability in all working conditions, the loop gain has to be compensated based on the worst case of control-to-output transfer function. However, in other conditions, the crossover frequencies of loop gain are sacrificed, resulting in poor transient responses. This paper proposes an adaptive variable-frequency peak current mode control with constant crossover frequency to mitigate the tradeoff between stability and transient response while possessing the variable frequency characteristic to improve light load efficiency. The adaptive control law is derived from the proposed small-signal model. Experimental and simulation results verify the analysis. The proposed control reduces the output voltage variation at load transient by 43% and 34% at 5 and 20 V output voltage, respectively.**

***Index Terms*—Adaptive variable-frequency peak current mode (AVFPCM) control, constant crossover frequency, flyback converter, universal serial bus power delivery (USB-PD).**

I. Introduction

FLYBACK converters with variable-frequency peak current mode (VFPCM) control are being widely adopted as a cost-effective isolated power converter for low power adapter applications [1], [2]. The VFPCM control is a common control method for flyback converters to meet the high efficiency requirement of the adapter over the entire load range [3]–[10]. Fig. 1 shows a practical frequency characteristic of VFPCM control. The switching frequency f_s decreases when the compensated voltage V_C decreases. Since V_C equals the sensed peak current of the switch, it is proportional to the output current.

Manuscript received April 12, 2018; revised June 11, 2018 and July 19, 2018; accepted September 3, 2018. Date of publication September 9, 2018; date of current version April 20, 2019. This work was supported by a research Grant 105-S-C29 from Richtek Corporation to Taiwan University, both in Taiwan. Recommended for publication by S. Kapat. *(Corresponding author: Ching-Jan Chen.)*

C.-H. Cheng and C.-J. Chen are with the Department of Electrical Engineering, National Taiwan University, Taipei 10617, Taiwan, R.O.C. (e-mail:

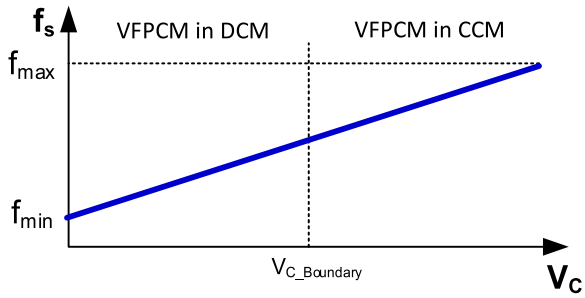

Fig. 1. Practical frequency characteristics of variable frequency control [9].

When the output current reduces, the switching frequency reduces to save energy, resulting in a higher light load efficiency. Quasi-resonant (QR) control is another common method to achieve high efficiency [11], [12]. However, in order to keep valley switching, the QR control may force the switching frequency to increase at light load, thus decreasing the light load efficiency. Primary side regulation (PSR) is also a popular control technique used in flyback converters [13]–[19]. It provides the advantages of lower cost and standby power losses. However, the PSR control possesses inherent issues in voltage sensing accuracy and load transient response speed. Thus, VFPCM control is more commonly used for high-efficiency adapter applications.

Fig. 2 shows the simplified circuit diagram of a traditional VFPCM control for flyback converters [9]. A rectified dc source charges the input capacitor of the flyback converter. Then, the flyback converter generates a regulated dc output voltage V_O for load resistor R_L. L_m is the magnetizing inductor of transformer and I_D is the current of the diode. The output capacitor is represented as C_o in series with an equivalent series resistor (ESR) $R_{\rm Co}$. The output voltage is sensed through an isolated type-II compensator consisting of an optocoupler and a TL431 to generate the compensated voltage V_C. In the controller, the compensated voltage V_C, the current signal $V_{\rm CS}$ sensed by $R_{\rm CS}$, and the slope compensation S_e determine the ON-time. Compared with the constant-frequency peak current mode (CFPCM) control, the compensated voltage V_C of VFPCM control determines not only the ON-time but also the switching frequency.

Recently, universal serial bus power delivery (USB-PD) specification has been proposed for adapter application [20]–[22].

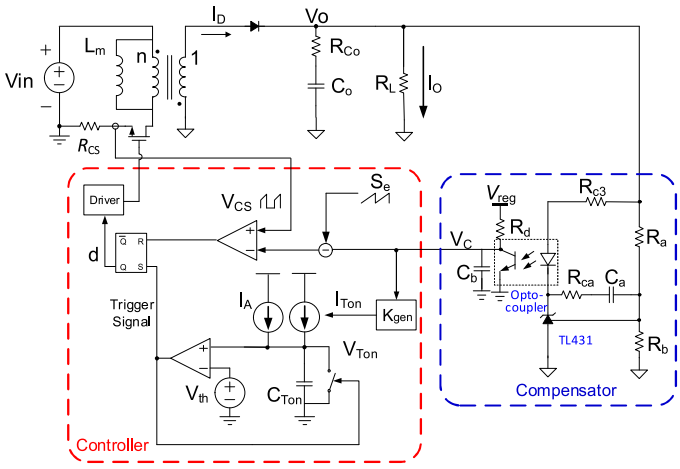

Fig. 2. Simplified circuit diagram of traditional VFPCM control for flyback converter [9].

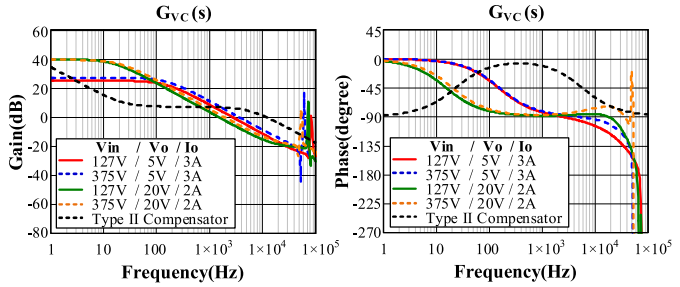

Fig. 3. $G_{\mathrm{VC}}(s)$ of traditional VFPCM control in various operation range of the USB-PD application.

An adapter with the USB-PD specification has the advantage of being able to supply to various devices. For example, it can provide a 5-V dc output voltage for cellphone load and a 19-V dc output voltage for laptop computer load. However, the wide output voltage range operation of USB-PD application makes the control-to-output transfer function $G_{\mathrm{vc}}(s)$ of the flyback converter vary under different working conditions.

It is not easy to stabilize the loop gain without sacrificing the transient response for conventional VFPCM control in the USB-PD application. Fig. 3 shows the $G_{\mathrm{vc}}(s)$ Bode plot of a traditional VFPCM control for 40 W USB-PD application. Apparently, in different working conditions, including universal line voltage change, output voltage change, and load current change in the USB-PD application, $G_{\mathrm{vc}}(s)$ varies significantly. Since loop gain $T(s)$ equals the multiplication of $G_{\mathrm{vc}}(s)$ and the compensator transfer function, it also varies at different operating conditions resulting in a possible stability issue during the most unfavorable conditions.

In order to stabilize the system, small-signal modeling techniques have been proposed to predict the stability of the flyback converter. The average modeling technique [24] is an easy method to predict the frequency response of the switching converters. However, one common problem with the average models is that they fail to predict subharmonic oscillations caused by the unstable current loop in CFPCM control. Thus, Ridley

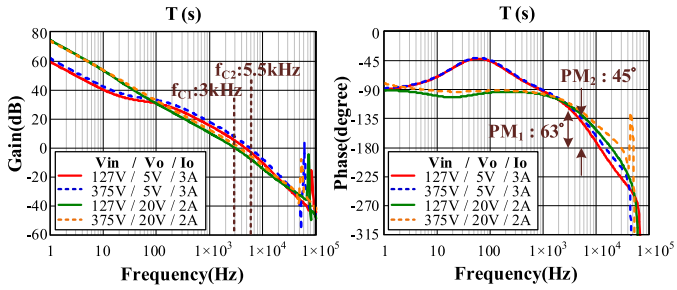

Fig. 4. Loop gains of traditional VFPCM control in various operation range of the USB-PD application.

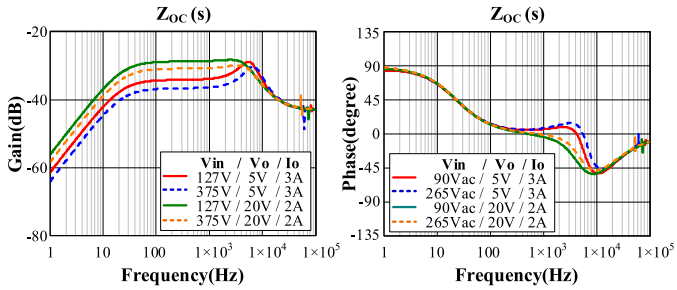

Fig. 5. Closed-loop output impedances of traditional VFPCM control in various operation range of the USB-PD application.

[25] presented a combination model, which can accurately predict subharmonic oscillations, based on the sample data model and the three-terminal switch model. Moreover, Chen [26] also successfully implemented the combination model to predict the CFPCM-controlled flyback converter. Even so, the combination model cannot accurately predict the frequency response of the variable-frequency control. In order to accurately predict the stability for different modulation schemes and implementation methods for current mode control, Li and Lee [27] proposed a describing function method. According to this approach, the authors in [9] and [10] proposed the complete small-signal model of the VFPCM controlled flyback converter and the compensation strategy to ensure stability for USB-PD application. However, it is not an easy task to ensure converter stability in all working conditions. Besides, the loop gain has to be compensated based on the worst case of $G_{\mathrm{vc}}(s)$ with the largest crossover frequency f_C. In other conditions, however, the crossover frequencies of $T(s)$ are sacrificed, resulting in poor load transient responses.

Figs. 4–6 show an example of worst-case compensation that ensures stability at the expense of slower transient response and larger output capacitance requirement. Fig. 4 shows the loop gain $T(s)$ compensated by considering the worst case of $G_{\mathrm{vc}}(s)$. Although the phase margins are greater than 45° in all the conditions, the crossover frequencies of others conditions are lower than that of the worst case. Therefore, the load transient responses of others conditions would be sacrificed since the closed-loop output impedances are directly affected by crossover frequencies of loop gains as shown in Fig. 5.

Fig. 6 shows that when the converter operates with an input voltage 127 V and output voltage 5 V, the peak-to-peak output

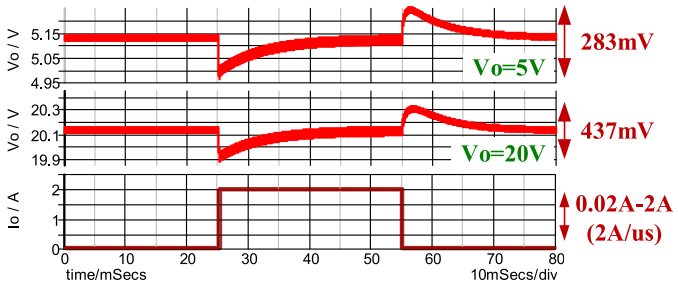

Fig. 6. Load transient waveforms of traditional VFPCM control in $V_{\text{in}} = 127$ V of the USB-PD application.

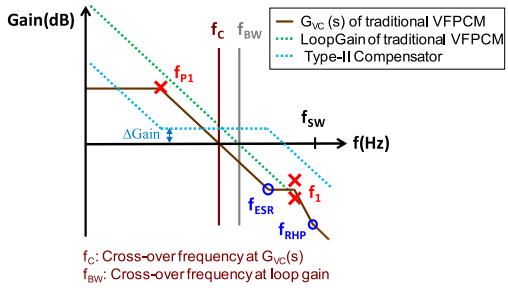

Fig. 7. Bode plot of compensator design for flyback converter with traditional VFPCM control.

voltage at load transient is 283 mV. When output voltage changes to 20 V, the crossover frequency of $T(s)$ decreases, resulting in an increased peak-to-peak output voltage of 437 mV. Thus, larger output capacitance is required to suppress the increased peak-to-peak output voltage, which increases the cost and board area. On the other hand, if the crossover frequency of $G_{\text{vc}}(s)$ can be fixed, the compensated $T(s)$ would not exhibit lower crossover frequencies in various conditions. That is to say, the load transient responses in various working conditions would be improved.

In this study, an adaptive VFPCM (AVFPCM) control with a constant crossover frequency f_C is proposed to improve the load transient response and to ease the design for stability of the wide-operation-range flyback converter such as USB-PD application. First, the reason for loop gain crossover frequency variation of traditional VFPCM control is analyzed in Section II. It is found that the traditional VFPCM control requires complex circuits and higher costs to implement constant crossover frequency by the analog control. In Section III, an AVFPCM control is proposed to achieve constant crossover frequency by analog control while possessing variable frequency characteristic to improve the light load efficiency. Furthermore, an accurate small-signal model for AVFPCM is also proposed. Based on this model, the adaptive control law is proposed to achieve a nearly constant and maximum crossover frequency of the loop gain, and to maintain the phase margins greater than 45° in all conditions. Thus, it improves the load transient response without sacrificing the stability for wide-operation-range flyback converter such as USB-PD application. Simulation and experimental verifications are demonstrated in Section IV. Compared to the traditional VFPCM control, the load transient responses of the proposed control are improved definitively from 283 to 158 mV and from 437 to 272 mV at output voltages 5 and 20 V, respectively. Finally, conclusions are presented in Section V.

II. Explanation of Loop Gain Crossover Frequency Variation in Traditional VFPCM Control

Fig. 7 shows a typical Bode plot of compensator design for flyback converter with traditional VFPCM control. $G_{\text{vc}}(s)$ is the control-to-output transfer function of the flyback converter, where its crossover frequency is defined as f_C. The crossover frequency of loop gain is defined as f_{BW}. Since $G_{\text{vc}}(s)$ is a transfer function with three poles and two zeros [9], the type-II compensator is proper to compensate it [23]. In the compensator design, the low-frequency zero of the compensator is set to cancel the low-frequency pole of $G_{\text{vc}}(s)$. The high-frequency pole of the compensator is placed beyond f_{BW} to suppress high-frequency noise. Besides, f_{BW} is lower than f_{ESR}, f_{p1}, and f_{RHP}. Therefore, the loop gain is presented as -20 dB/dec through the crossover frequency.

As shown in Fig. 7, it is clear that f_{BW} of loop gain is only affected by f_C when the compensator is fixed. Since the loop gain is compensated as -20 dB/dec line through crossover frequency, the relation of f_{BW} and f_C can be described as (1), where ΔGain is the middle-frequency gain of the compensator. From (1), f_{BW} can be further presented as (2). Since ΔGain is constant for the same compensator, f_{BW} is only affected by f_C, as shown in the following:

$$\frac{\Delta\text{Gain}}{\log f_{\text{BW}} - \log f_C} = -20\,(\text{dB/dec}) \tag{1}$$

$$f_{\text{BW}} = 10^{\log f_C - \frac{\Delta\text{Gain}}{20}}. \tag{2}$$

Since only a low-frequency pole of $G_{\text{vc}}(s)$ is lower than f_C, f_C can be simplified by multiplying the dc gain and low-frequency pole of $G_{\text{vc}}(s)$. Based on the $G_{\text{vc}}(s)$ transfer function in [9] and the definition of the decibel unit, the unity gain of $G_{\text{vc}}(s)$ happens at crossover frequency ω_C as shown in (3). According to the compensated result in Fig. 7, (3) can be approximated to (4). Based on (4), f_C is derived as (5). From (5), f_C is further approximated as (6) since $G_{\text{VC\_DC}}$ is much greater than 1.

$$|G_{\text{VC}}(j\omega_C)| = 1$$

$$= G_{\text{VC\_DC}} \sqrt{\frac{\left[1^2 + \left(\frac{\omega_C}{\omega_{\text{ESR}}}\right)^2\right]\left[1^2 + \left(\frac{\omega_C}{\omega_{\text{RHP}}}\right)^2\right]}{\left[1^2 + \left(\frac{\omega_C}{\omega_{P1}}\right)^2\right]\left[\left(1^2 - \frac{\omega_C{}^2}{\omega_1{}^2}\right)^2 + \left(\frac{\omega_C}{Q_1\omega_1}\right)^2\right]}} \tag{3}$$

$$|G_{\text{VC}}(j\omega_C)| = 1 \cong G_{\text{VC\_DC}} \sqrt{\left[1^2 + \left(\frac{\omega_C}{\omega_{P1}}\right)^2\right]^{-1}} \tag{4}$$

$$f_C = \frac{\omega_C}{2\pi} \cong \frac{\omega_{P1}}{2\pi}\sqrt{G_{\text{VC\_DC}}{}^2 - 1^2} \tag{5}$$

$$f_C \cong \frac{\omega_C}{2\pi} = \frac{1}{2\pi} G_{\text{VC\_DC}}\omega_{P1}. \tag{6}$$

The f_C variation of traditional VFPCM control and the possibility to achieve invariant f_C over a wide operation range are investigated in the following. By substituting $G_{\text{VC\_DC}}$ and ω_{p1} of traditional VFPCM control [9] into (6), f_C can be presented as (7). Then (7) is further simplified to (8) as R_{Co} is usually much smaller than load resistor R_L and $k_2 \cdot R_{\text{Co}}$ is much less than 1 in practical applications. Equation (8) shows that f_C varies with different input and output voltages. Furthermore, it also changes with the output current since the switching period depends on it. Namely, f_{BW} of loop gain and load transient response vary in different operating conditions

$$\begin{aligned} f_C &\cong \frac{G_{\text{VC\_DC}}\omega_{P1}}{2\pi} \\ &= \frac{1}{2\pi}\left(\frac{DK_{\text{gen}}T_S{}^2(2S_e + S_n)}{2V_{\text{th}}C_{\text{Ton}}} + 1\right) \\ &\quad \times \frac{1}{R_{\text{CS}}}\frac{DV_{\text{in}}}{V_O}\frac{R_L}{C_o(R_{\text{Co}} + R_L)}\frac{1}{\left(1 - k_2\frac{R_L R_{\text{Co}}}{R_{\text{Co}} + R_L}\right)} \end{aligned} \tag{7}$$

$$f_C \cong \frac{1}{2\pi}\left(\frac{DK_{\text{gen}}T_S{}^2(2S_e + S_n)}{2V_{\text{th}}C_{\text{Ton}}} + 1\right)\frac{DV_{\text{in}}}{V_O}\frac{1}{R_{\text{CS}}}\frac{1}{C_o} \tag{8}$$

where

$$S_n = R_{CS} \cdot \frac{V_{\text{in}}}{L_m}, S_f = R_{CS} \cdot \frac{nV_O}{L_m}.$$

According to (8), if f_C can be fixed by adaptively adjusting the parameters of the control circuit such as K_{gen} and V_{th}, f_{BW} can be kept constant and the load transient response in various operation conditions can be improved. However, achieving a constant f_C for traditional VFPCM control is more expensive as a multiplier is required to obtain the square of the switching period signal by analog control. In order to achieve a constant f_C, this study proposes an AVFPCM control which does not need additional external components and multiplier.

III. Proposed AVFPCM Control, Small-Signal Model, and Adaptive Control Law for Constant Crossover Frequency

A. Proposed AVFPCM Control

Fig. 8 shows the simplified circuit diagram of an AVFPCM-controlled flyback converter, which can implement constant crossover frequency control by analog control and simple circuit. Compared with the traditional VFPCM control, the switching frequency of the AVFPCM is not varied by the bias current I_{Ton} but by the threshold voltage V_F. A voltage gain K_{gen} is used for changing the frequency and an extra voltage gain K_a is inserted into the pulsewidth modulation (PWM) loop to add a degree of freedom for designing the operational voltage of V_C. Additionally, K_{out} and K_{in}, two voltage-controlled current sources, make the current source I_A and the external ramp

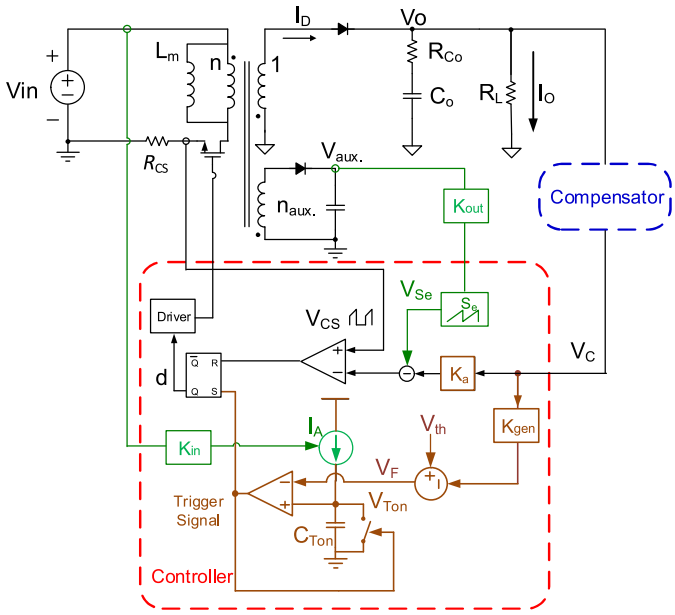

Fig. 8. Simplified circuit diagram of proposed AVFPCM control with constant crossover frequency.

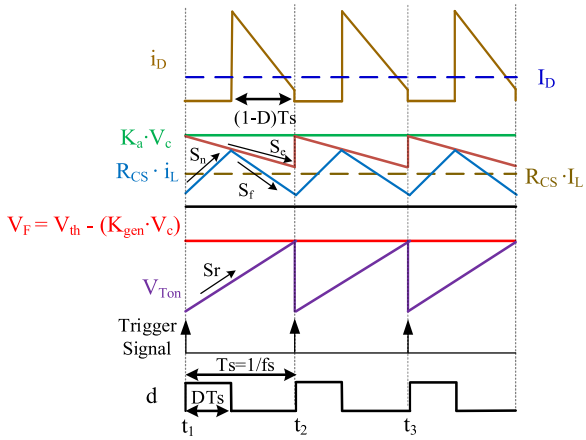

Fig. 9. Steady-state waveforms of NVFPCM control in CCM.

slope S_e change adaptively with the input voltage and the auxiliary winding voltage V_{aux}, respectively, to achieve a constant crossover frequency.

Fig. 9 shows the steady state waveforms of AVFPCM in CCM. When the voltage V_{Ton} of the capacitor C_{Ton} is charged to V_F, a new switching cycle starts. Since V_F is inversely related to $K_{\text{gen}} \cdot V_C$, switching frequency f_S is determined by V_C. Moreover, the turn OFF instant of duty cycle is determined by the sensed inductor current. When $i_L \cdot R_{\text{CS}}$ reaches $K_a \cdot V_C$ minus slope compensation S_e, the duty cycle turns OFF. When output current I_O decreases, V_C and switching frequency also decrease. Therefore, the proposed control also achieves frequency reduction function to increase the light load efficiency.

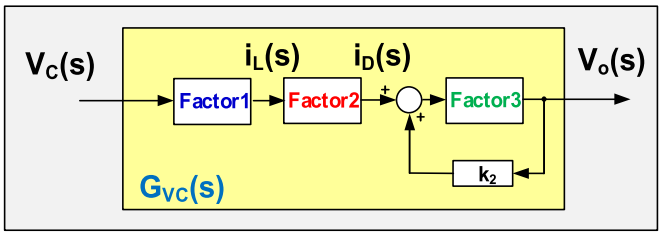

Fig. 10. Control block diagram of AVFPCM control.

B. Small-Signal Model of Proposed AVFPCM Control

The modeling strategy for AVFPCM control is the same as that for traditional VFPCM control in [9]. As shown in Fig. 10, the control-to-output transfer function $G_{\rm vc}(s)$, defined as $v_o(s)/v_c(s)$, can be expressed by three main transfer functions, namely Factor1(s), Factor2(s), and Factor3(s) in the mathematical derivation. The AVFPCM control contains highly nonlinear signal of inductor current and variable frequency operation. Thus, the describing function approach [27] is used to accurately model the nonlinear part of the control. The nonlinear part of the control such as inductor, switch, and modulation circuit are modeled as a single entity blocked by Factor1. Then, Factor2 and Factor3 are modeled by the average model [24].

As shown in Fig. 10, the control-to-output transfer function $G_{\rm vc}(s)$ can be derived as in the following:

$$G_{\rm vc}(s) \equiv \frac{v_O(s)}{v_c(s)} = \text{Factor1}(s)\cdot\text{Factor2}(s)\cdot\frac{\text{Factor3}(s)}{1-k_2\text{Factor3}(s)}. \quad (9)$$

Factor1(s), which is derived by using the describing function approach [27], can be derived as (10). Since S_e is changed adaptively by the dc component of the output voltage in the proposed control, it is approximated to be a constant slope in the derivation of Factor1(s), as shown in the following:

$$\text{Factor1}(s) = \frac{i_L(s)}{v_c(s)} = \frac{\left(\frac{K_{\rm gen}C_{\rm Ton}D(2S_e+S_n)}{2I_A}+K_a\right)\left(1+\frac{s}{Q_3\omega_3}+\frac{s^2}{{\omega_3}^2}\right)}{R_{\rm CS}\left(1+\frac{s}{Q_1\omega_1}+\frac{s^2}{{\omega_1}^2}\right)\left(1+\frac{s}{Q_2\omega_2}+\frac{s^2}{{\omega_2}^2}\right)} \quad (10)$$

where unnumbered eqn. shown at bottom of this page.

It is worth mentioning that the Factor1(s) of the proposed control possesses the additional double pole and double zero compared with the traditional VFPCM control [9]. In the traditional VFPCM control, the high-frequency components of V_C are attenuated by $C_{\rm Ton}$ before inputting a variable frequency path. Thus, there are no extra sideband effects produced in PWM except the original sideband effects of the inductor current, which are produced by peak current control [28], [29]. However, in the proposed control, the high-frequency components of V_C directly inject into the PWM through a variable frequency path. Therefore, extra sideband frequency components appear on the frequency response as the high-frequency double pole and double zero shown in (10).

The Factor2(s) can be derived as given in the following using the average model approach, which gets the same result as [9]:

$$\text{Factor2}(s) = \frac{i_D(s)}{i_L(s)} = \frac{DV_{\rm in}}{V_O}\left[1-\frac{DL_m}{n^2(1-D)^2R_L}s\right]. \quad (11)$$

The Factor3(s) transfer function can be obtained from the output network impedance, which consists of the output capacitor and load resistor as

$$\text{Factor3}(s) = \frac{v_O(s)}{i_D(s)} = \frac{R_L\left(1+sC_oR_{\rm Co}\right)}{1+sC_o\left(R_{\rm Co}+R_L\right)}. \quad (12)$$

k_2 is derived by the average modeling approach [9]. The result is represented as

$$k_2 \cong \left.\frac{\hat{i}_D}{\hat{v}_O}\right|_{\hat{v}_c=0} = -\frac{n^2(1-D)^3T_S}{2L_m} - \frac{n(1-D)}{(V_{\rm in}+nV_O)} \times\left(\frac{V_O}{(1-D)R_L}+\frac{n}{R_{\rm CS}}S_e(1-D)T_S\right). \quad (13)$$

Finally, using the expression of Factor1(s) from (10), Factor2(s) from (11), Factor3(s) from (12), and k_2 from (13), (9) can be simplified as

$$G_{\rm VC}(s) = \frac{v_o(s)}{v_c(s)} \cong G_{\rm VC\_DC}\frac{\left(1+\frac{s}{\omega_{\rm ESR}}\right)\left(1-\frac{s}{\omega_{\rm RHP}}\right)\left(1+\frac{s}{Q_3\omega_3}+\frac{s^2}{{\omega_3}^2}\right)}{\left(1+\frac{s}{\omega_{P1}}\right)\left(1+\frac{s}{Q_1\omega_1}+\frac{s^2}{{\omega_1}^2}\right)\left(1+\frac{s}{Q_2\omega_2}+\frac{s^2}{{\omega_2}^2}\right)} \quad (14)$$

where the parameters are summarized in Table I.

$$Q_1 = \frac{1}{\pi\left(\frac{1}{2}+\frac{(S_e-S_f)}{(S_n+S_f)}\right)}, \quad \omega_1 = \frac{\pi}{T_S}, Q_2 = \frac{2}{\pi}, \omega_2 = \frac{\pi}{DT_S}$$

$$Q_3 = \frac{2\pi\sqrt{D\left[2K_a+A_1D\left(S_e+S_n\right)\right]\left[2K_aD+2A_1\left(S_n+S_e\right)+A_1DS_n\right]}}{D\left(4A_1S_n+4A_1S_nD+2\pi^2K_a+2\pi^2A_1S_e+\pi^2A_1S_n\right)}$$

$$\omega_3 = \frac{\pi}{T_S}\sqrt{\frac{2K_a+2A_1DS_e+A_1DS_n}{D\left[2K_aD+A_1DS_n+2A_1\left(S_e+S_n\right)\right]}}, \quad A_1 = \frac{K_{\rm gen}C_{\rm Ton}}{I_A}$$

TABLE I
TRANSFER FUNCTION PARAMETERS OF AVFPCM IN CCM

Item	AVFPCM in CCM
G_{VC_DC}	$\left(\frac{K_{gen}C_{Ton}D(2S_e+S_n)}{2I_A}+K_a\right)\frac{1}{R_{CS}}\frac{DV_{in}}{V_O}\frac{R_L}{(1-k_2R_L)}$
ω_{P1}	$\frac{1}{C_o(R_{Co}+R_L)}\frac{(1-k_2R_L)}{\left(1-k_2\frac{R_LR_{Co}}{R_{Co}+R_L}\right)}$
ω_{ESR}	$\frac{1}{R_{Co}C_o}$
ω_{RHP}	$\frac{(1-D)^2n^2R_L}{DL_m}$
Q_1	$\frac{1}{\pi\left(\frac{1}{2}+\frac{(S_e-S_f)}{(S_n+S_f)}\right)}$
ω_1	π/T_S
Q_2	$2/\pi$
ω_2	π/DT_S
Q_3	$\frac{2\pi\sqrt{D\left[2K_a+A_1D(S_e+S_n)\right]\left[2K_aD+2A_1(S_n+S_e)+A_1DS_n\right]}}{D\left(4A_1S_n+4A_1S_nD+2\pi^2K_a+2\pi^2A_1S_e+\pi^2A_1S_n\right)}$
ω_3	$\frac{\pi}{T_S}\sqrt{\frac{2K_a+2A_1DS_e+A_1DS_n}{D\left[2K_aD+A_1DS_n+2A_1(S_e+S_n)\right]}}$
A_1	$K_{gen}C_{Ton}/I_A$
D	$\frac{nV_O}{V_{in}+nV_O}$
k_2	$-\frac{n^2(1-D)^3T_S}{2L_m}-\frac{n(1-D)}{(V_{in}+nV_O)}\left(\frac{V_O}{(1-D)R_L}+\frac{n}{R_{CS}}S_e(1-D)T_S\right)$

C. Adaptive Control Law for Constant Crossover Frequency

Based on the derived small-signal model of AVFPCM, the adaptive control law is proposed in this section to achieve a constant crossover frequency f_C. First, the f_C equation of proposed AVFPCM control is derived as given in the following by substituting $G_{\mathrm{VC\_DC}}$ and ω_{p1} of Table I into (6):

$$f_{\mathrm{C}} \cong \frac{G_{\mathrm{VC\_DC}}\omega_{P1}}{2\pi} = \frac{1}{2\pi}\left(\frac{K_{\mathrm{gen}}C_{\mathrm{Ton}}D(2S_e+S_n)}{2I_A}+K_a\right) \times \frac{1}{R_{\mathrm{CS}}}\frac{DV_{\mathrm{in}}}{V_O}\frac{R_L}{C_o(R_{\mathrm{Co}}+R_L)}\frac{1}{\left(1-k_2\frac{R_LR_{\mathrm{Co}}}{R_{\mathrm{Co}}+R_L}\right)}. \quad (15)$$

Then, using the approximation that R_L is much greater than R_{Co} and $k_2 \cdot R_{\mathrm{Co}}$ is much less than 1, f_C of AVFPCM can be simplified as

$$f_C \cong \frac{1}{2\pi}\left(\frac{K_{\mathrm{gen}}C_{\mathrm{Ton}}D(2S_e+S_n)}{2I_A}+K_a\right)\frac{DV_{\mathrm{in}}}{V_O}\frac{1}{R_{\mathrm{CS}}}\frac{1}{C_o}. \quad (16)$$

From (16), it is found that if twice S_e is equal to S_f as (17), then f_C of AVFPCM can be simplified as (18). According to (18), f_C varies with the input voltage and output voltage due to the duty-cycle term appearing in the equation. If (19) is achieved, constant f_C can be achieved because the term in (18), which when multiplied by the duty cycle D, is equal to zero, as shown in the following:

$$2S_e = S_f \quad (17)$$

$$f_C \cong \frac{1}{2\pi}\left(\frac{2I_AK_an+nD(K_{\mathrm{gen}}C_{\mathrm{Ton}}S_n-2I_AK_a)}{2I_A}\right)\frac{1}{R_{\mathrm{CS}}}\frac{1}{C_o} \quad (18)$$

$$K_{\mathrm{gen}}C_{\mathrm{Ton}}S_n - 2I_AK_a = 0. \quad (19)$$

Therefore, the purpose of the control law is to design the circuit parameter by fulfilling (17) and (19) to achieve constant f_C. After parameters such as n, K_a, R_{cs}, and C_O are decided, f_C of AVFPCM can be kept constant as (20), which does not change with the input voltage, output voltage, switching frequency, or output current. Namely, constant crossover frequency over wide operation range can be achieved by

$$f_C \cong \frac{G_{\mathrm{VC\_DC}}\omega_{P1}}{2\pi} = \frac{1}{2\pi}\frac{nK_a}{R_{\mathrm{CS}}}\frac{1}{C_o}. \quad (20)$$

D. Circuit Implementation of Adaptive Control Law

To implement the adaptive control law, (17) and (19) can be further derived as given in the following:

$$S_e = \frac{S_f}{2} = \frac{nR_{\mathrm{CS}}}{2L_m}V_O \quad (21)$$

$$I_A = \frac{K_{\mathrm{gen}}C_{\mathrm{Ton}}}{2K_a}\frac{R_{\mathrm{CS}}}{L_m}V_{\mathrm{in}}. \quad (22)$$

In practical applications, an auxiliary winding is often employed to supply energy for control IC. This supply voltage V_{aux} is proportional to the dc output voltage by turns ratio n_{aux} as shown in (23). According to (23), (21) can be expressed as (24). Therefore, constant crossover frequency is achieved if (22) and (24) are achieved. That is to say, S_e and I_A are proportional to V_{aux} and input voltage V_{in} respectively, as shown in the following:

$$V_O = \frac{V_{\mathrm{aux.}}}{n_{\mathrm{aux.}}} \quad (23)$$

$$S_e = \frac{S_f}{2} = \frac{nR_{\mathrm{CS}}}{2L_mn_{\mathrm{aux.}}}V_{\mathrm{aux.}}. \quad (24)$$

As shown in Fig. 8, the current source I_A is adaptive to input voltage with a gain of K_{in} and the external ramp slope S_e is adaptive to auxiliary winding voltage V_{aux} with a gain of K_{out} to achieve constant f_C. Besides, the gain blocks K_{in} and K_{out} have

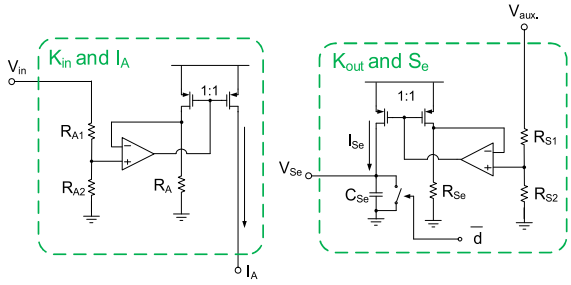

Fig. 11. Proposed circuit diagrams of K_{in} and K_{out} blocks of the AVFPCM control.

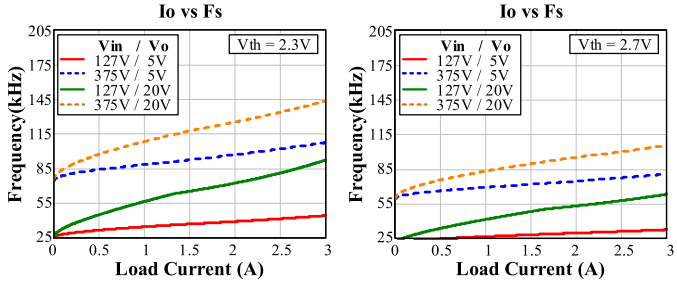

Fig. 12. Switching frequency versus I_O of the adaptive AVFPCM control with constant crossover frequency in USB-PD application range.

to achieve the following, respectively, to achieve the adaptive control law (22) and (24):

$$K_{\text{in}} \triangleq \frac{I_A}{V_{\text{in}}} = \frac{K_{\text{gen}} C_{\text{Ton}}}{2K_a} \frac{R_{\text{CS}}}{L_m} \tag{25}$$

$$K_{\text{out}} \triangleq \frac{S_e}{V_{\text{aux.}}} = \frac{nR_{\text{CS}}}{2L_m n_{\text{aux.}}}. \tag{26}$$

Fig. 11 shows the circuit diagrams of K_{in} and K_{out} blocks. By using divided resistors R_{A1} R_{A2}, R_{S1}, and R_{S2}, the gains of K_{in} and K_{out} can be realized easily. Moreover, by using a current mirror, unity-gain buffer, and resistor R_A, R_{Se}, the input voltages of K_{in} and K_{out} blocks can be transformed into currents to charge the capacitors to determine the switching frequency and to achieve slope compensation, respectively.

Since the state-of-the-art control IC usually possesses the auxiliary winding voltage and input voltage information, the proposed control does not require additional external components to achieve constant f_C if K_{in} and K_{out} are implemented into the IC. Besides, the adaptive circuits can be easily integrated into the IC since they are only composed of current mirror, buffer, and resistor.

E. Frequency Reduction Characteristic of Proposed AVFPCM Control with Constant Crossover Frequency

In AVFPCM control, the frequency reduction characteristic, which is essential for efficiency optimization and control IC parameter design, is closely related to bias current I_A. Therefore, the frequency reduction characteristic is analyzed when I_A is varied to achieve constant f_C. Based on the CCM waveforms in Fig. 9, the average diode current I_D, which equals the output current I_O at steady state, can be obtained as (27). Here, 100% converter efficiency is assumed for simplicity. The relation between V_C and switching period T_S is described by (28) according to the capacitor charge equation. Moreover, in order to achieve constant f_C, S_e and I_A require to satisfy (21) and (22). By substituting (21), (22), and (28) into (27), the switching frequency f_S is derived out as (29), which shows the relation between f_S and I_O.

The derived switching frequency f_S in (29) shows the frequency reduction characteristic that f_S decreases at light load. Fig. 12 shows f_S versus I_O relation of AVFPCM control with constant crossover frequency in USB-PD application range with different V_{th}. Moreover, it also shows that V_{th} can adjust the frequency reduction characteristic effectively. Obviously, V_{th} provides a degree of freedom for designing the frequency reduction function at different working conditions. Besides, based on (20), adjusting V_{th} does not affect the constant crossover frequency control

$$I_O = I_D = \frac{n(1-D)}{2R_{\text{CS}}} \left[2\left(V_C - S_e D T_S\right) - S_f (1-D) T_S\right] \tag{27}$$

$$T_S I_A = \left(V_{\text{th}} - K_{\text{gen}} V_C\right) C_{\text{Ton}} \tag{28}$$

$$f_S = \frac{n(1-D)(S_n + S_f)}{2R_{\text{CS}}} \left(\frac{n(1-D) K_a}{R_{\text{CS}} K_{\text{gen}}} V_{\text{th}} - I_O\right)^{-1}. \tag{29}$$

F. Stability Discussion of Current Loop in Proposed AVFPCM Control with Constant Crossover Frequency

Since the stability of the current loop relates to slope compensation S_e closely, it is necessary to discuss the stability of the current loop in the application range while S_e is varied to achieve constant f_C. Based on the above small-signal mode of AVFPCM, Q_1 can estimate the stability of the current loop. Substituting (21) into the Q_1 equation in Table I, Q_1 of AVFPCM control with constant crossover frequency can be expressed as (30). Obviously, Q_1 of the constant crossover frequency control varies with the input and output voltages. In order to confirm the stability of the current loop in the USB-PD application, the magnitude of Q_1 of the constant crossover frequency control is illustrated in Fig. 13 for various conditions with circuit parameters listed in Table II. As shown in Fig. 13, the maximum and minimum values of Q_1 are 1.25 and 0.68, respectively, so the current loop is always stable for the USB-PD application, as shown in the following:

$$Q_{1,\text{constant\_fc}} = \frac{1}{\pi\left(\frac{1}{2} + \frac{(S_e - S_f)}{(S_n + S_f)}\right)} = \frac{1}{\pi\left(\frac{1}{2} + \frac{(\frac{S_f}{2} - S_f)}{(S_n + S_f)}\right)} = \frac{2(V_{\text{in}} + nV_O)}{\pi V_{\text{in}}}. \tag{30}$$

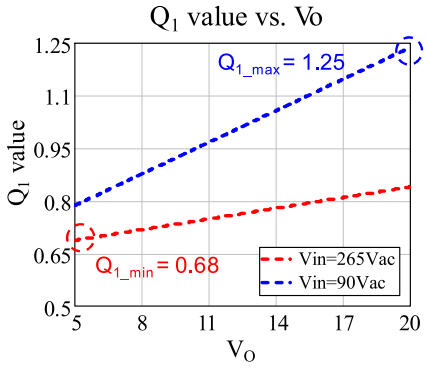

Fig. 13. Q_1 magnitude of the NVFPCM control with constant crossover frequency in USB-PD application range.

TABLE II
CIRCUIT PARAMETERS OF EXPERIMENT AND SIMULATION

Item	NVFPCM in CCM			
Input voltage	127 V (Vac=90 Vrms)		375 V (Vac=265 Vrms)	
Output voltage	5 V	20 V	5 V	20 V
Output current	3 A	2 A	3 A	2 A
Switching frequency f_S	44 kHz	80 kHz	95 kHz	114 kHz
Magnetic inductor L_m	1.2 mH			
Transformer turn ratio n	6.3			
Output capacitor C_o	1360 µF			
ESR of capacitor R_{Co}	7 mΩ			
Slope compensation S_e	6.7 V/mS	26.8 V/mS	6.7 V/mS	26.8 V/mS
Bias current I_A	40.5 uA	40.5 uA	119.5 uA	119.5 uA
Reference design	K_{in}= 32 uA/V, K_{out}= 121 A/V K_{gen}= 0.5 A/V, K_a= 0.33 V/V Rcs = 0.51 Ω, C_{Ton} = 1 nF, V_{th} = 2.3 V			
Compensator design	R_a= 68 kΩ, R_{ca}=1 kΩ R_{c3} = 600 Ω, R_d=20 kΩ C_a = 100 nF, C_b = 1.8 nF			
Low-side divided resistor R_b	68 kΩ	9.7 kΩ	68 kΩ	9.7 kΩ
Opto-coupler current gain	50%			

IV. SIMULATION AND EXPERIMENTAL RESULTS

The transfer functions $G_{vc}(s)$, $T(s)$, $Z_{OC}(s)$, and load transient responses are verified by SIMPLIS simulation tool. The simulation accuracy of SIMPLIS is widely proven in many power electronics studies [27]–[32]. The circuit parameters and working conditions for experiment and simulation are listed in Table II, where R_b is varied to achieve different output voltages. Moreover, the slope compensation S_e and bias current I_A vary with the operating condition due to the adaptive law. Fig. 14 shows $G_{vc}(s)$ of proposed AVFPCM control with constant crossover frequency in various conditions. As SIMPLIS simulation results present, the gains of $G_{vc}(s)$ in various conditions are concentrated into a -20 dB/dec slash line through the same crossover frequency. Apparently, the performance of the proposed control achieves constant crossover frequency in various working conditions.

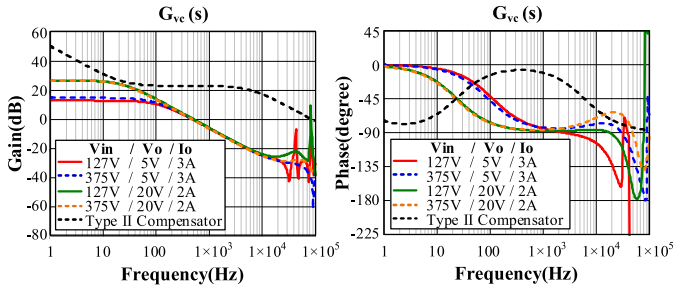

Fig. 14. Performance verification of AVFPCM control by simulation.

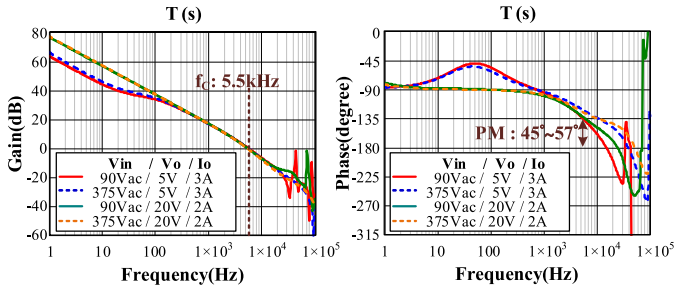

Fig. 15. Loop gain simulation of AVFPCM control with constant crossover frequency in various conditions.

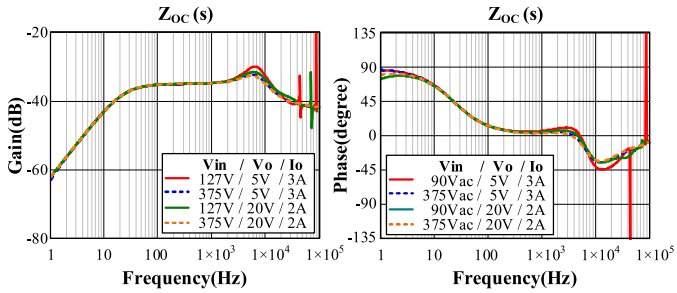

Fig. 16. Closed-loop output impedance simulation of AVFPCM control with constant crossover frequency in various conditions.

Figs. 15 and 16 show the simulated loop gains and closed-loop output impedances of the proposed control in various conditions while the compensators are kept the same. The simulation conditions and compensator parameters are the same as that in Table II. The SIMPLIS simulation results show that the crossover frequencies of $T(s)$ are fixed at 5.5 kHz and phase margins are greater than 45° in all conditions. In addition, $Z_{OC}(s)$ before the crossover frequency of $T(s)$ are concentrated into a line. In other words, the proposed control achieves constant crossover frequency to improve load transient responses effectively without sacrificing the system stability for the USB-PD application. Compared to the peak-to-peak output voltage variation at load transient shown in Fig. 6, the load transient responses of proposed control shown in Fig. 17 are improved definitively from 283 to 158 mV and from 437 to 272 mV at output voltages 5 and 20 V, respectively. In addition, the influence of variation of the circuit parameters on the performance of the proposed control is also checked. Even when there are $\pm 25\%$ mismatches

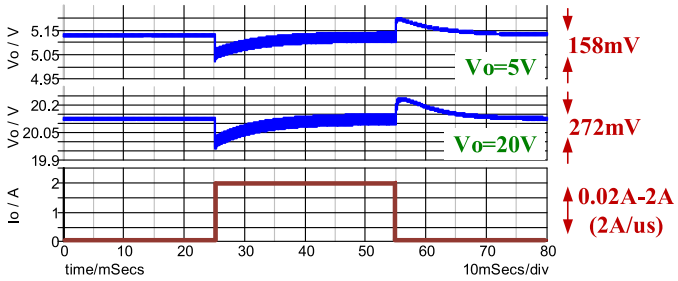

Fig. 17. Load transient response simulation of AVFPCM control with constant crossover frequency in $V_{\text{in}} = 127$ V of the USB-PD application.

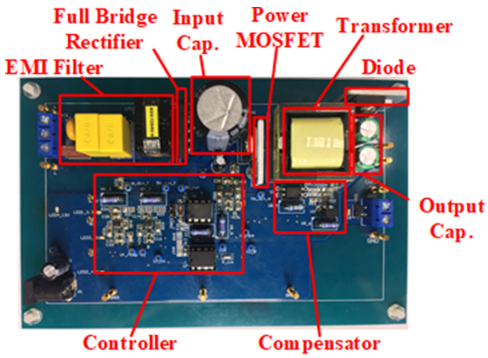

Fig. 18. Prototype flyback converter.

appearing in the implementation of the gains of K_{in} and K_{out}, the variations in the crossover frequencies are maintained lower than 100 Hz. The verification is not presented here owing to page restrictions.

An experimental platform for the flyback converter with the proposed control is built as shown in Fig. 18. The control circuit is built with an analog peak current mode controller, UC3843. The UC3843 provides a frequency setting pin for the user to adjust the switching frequency, thus the variable-frequency control can be implemented by this pin as shown in Fig. 19. The K_{in} and K_{out} blocks of the proposed control are achieved by an ADL5315 from Analog Devices as the voltage-controlled current source to implement bias current I_A and slope compensation S_e, an ADA4891 as the amplifiers to implement the operational amplifier and K_{gen}. In addition, an LM393 as the comparator generates the trigger signal to determine the switching frequency. The test parameters and working conditions for the experiments are the same as the simulation parameters listed in Table II.

Figs. 20 and 21 are the measured load transient waveforms of flyback converter with the proposed control operated at 5 V and 20 V output voltages, respectively. When output current changes from 0.02 to 2 A, the peak-to-peak output voltage variation in 5 and 20 V conditions are 160 and 288 mV, respectively. These results are very close to the simulation results. Besides, the proposed control reduces the output voltage variation by 43% and 34%, respectively, in the 5 and 20 V conditions compared to the traditional VFPCM control shown in Fig. 6. The voltage ripple is larger in high load current or high output voltage condition

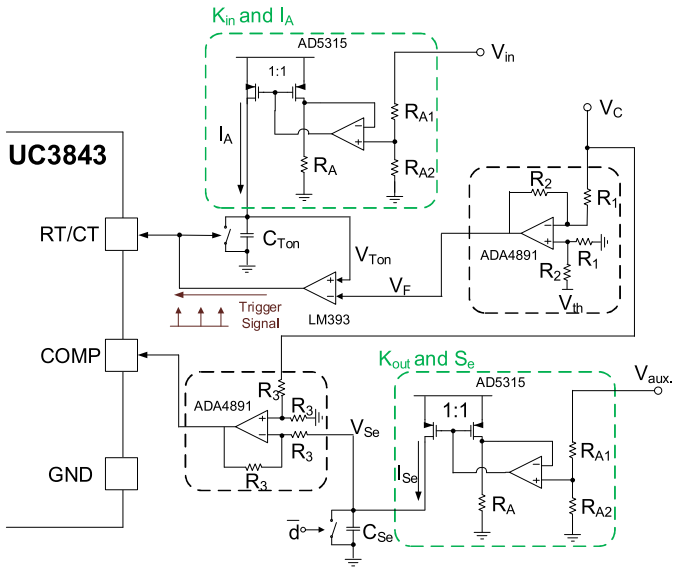

Fig. 19. AVFPCM control implementation by UC3843.

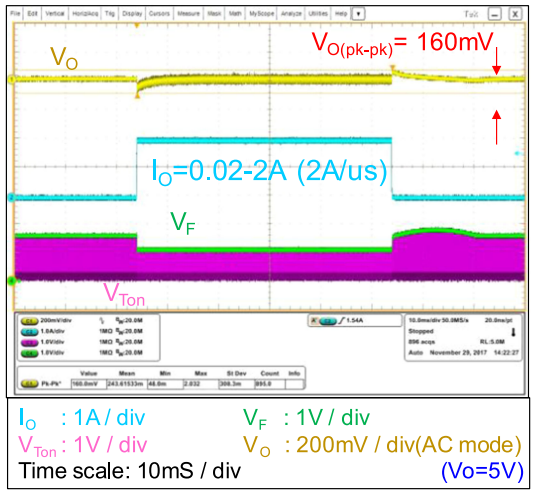

Fig. 20. Load transient waveforms of proposed control ($V_{\text{in}} = 127$ V and $V_o = 5$ V).

as predicted in the simulation due to the higher discontinuous diode current and diode reverse recovery current, respectively.

Figs. 22 and 23 show the zoom-in waveforms of Fig. 20 when the load current increases from light load to full load and then reduces to light load. When the output current varies from light load to full load, the switching frequency becomes higher with a decreased voltage of V_F. When the output current varies from full load to light load, the switching frequency reduces. Obviously, the proposed control possesses variable switching frequency performance.

Fig. 24 shows the efficiency comparison between the CFPCM control and the proposed control, where the frequency reduction characteristic of the latter is shown in Fig. 12, when V_{th} is set at 2.3 V. Clearly, the variable-frequency characteristic can improve the light load efficiency effectively. Especially for cases where switching losses dominate total power loss, such as high

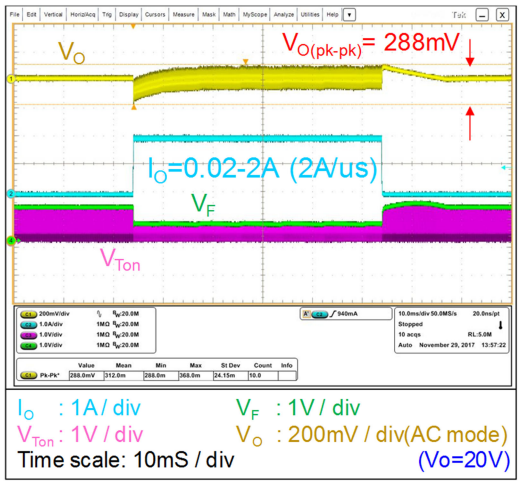

Fig. 21. Load transient waveforms of proposed control ($V_{\text{in}} = 127$ V and $V_o = 20$ V).

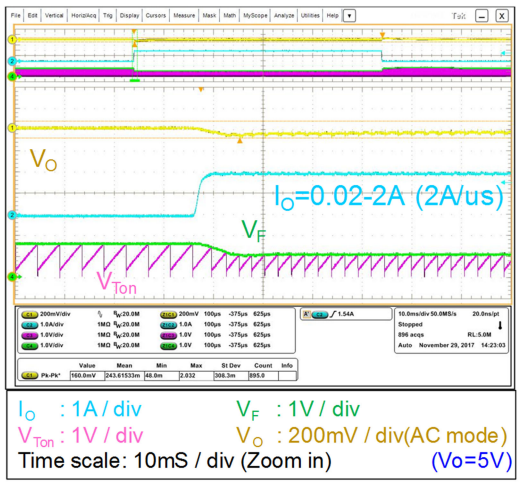

Fig. 22. Zoom in waveforms of load raising in Fig. 20.

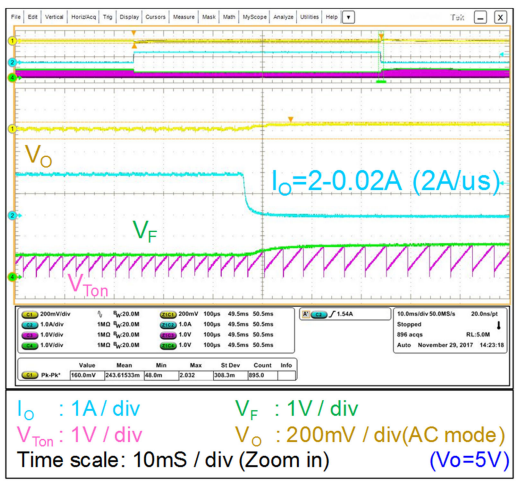

Fig. 23. Zoom in waveforms of load falling in Fig. 20.

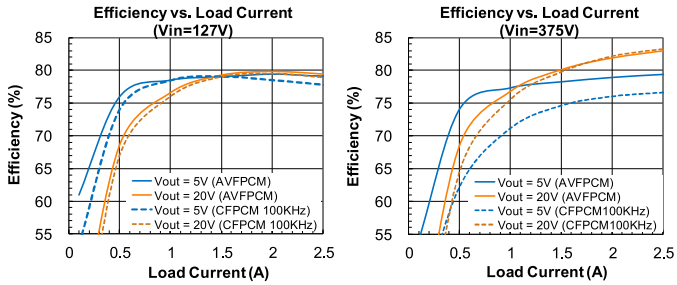

Fig. 24. Efficiency measurement of proposed control.

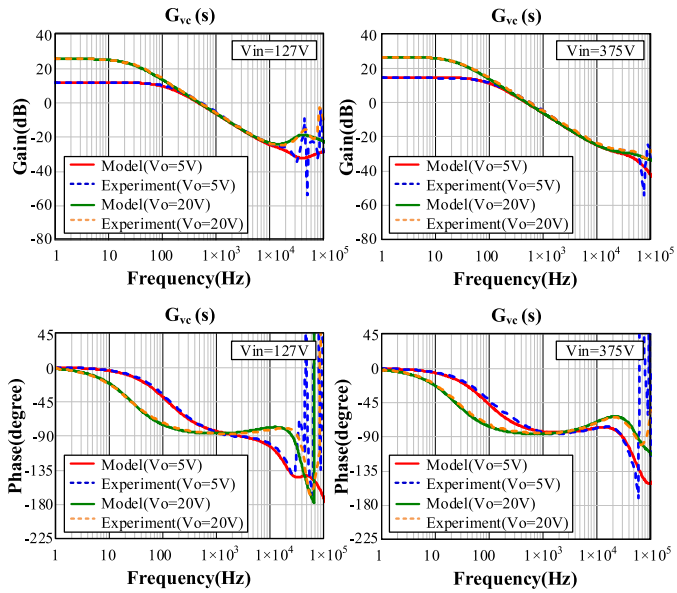

Fig. 25. Experimental verification of AVFPCM control model.

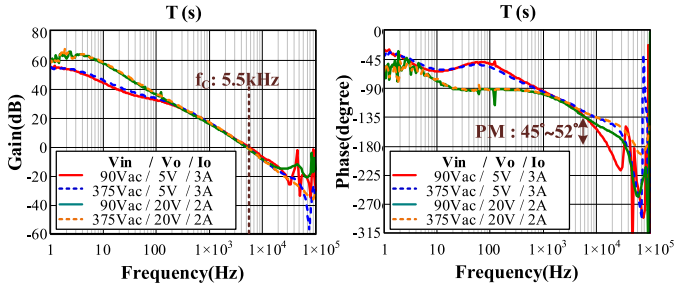

Fig. 26. Loop gain verification by experiment of proposed AVFPCM control with constant crossover frequency at wide operating range.

input voltage and low output voltage, the maximum efficiency improvement can be close to 5%.

Fig. 25 verifies the model of $G_{\text{vc}}(s)$ of AVFPCM control in various conditions. It indicates that the results of the proposed small-signal model are in excellent agreement with the measurements. Apparently, in comparison with Fig. 3, the change of $G_{\text{vc}}(s)$ of AVFPCM control in different working condition is reduced. Fig. 26 shows the measurement results of loop gains of the proposed control. It is shown that constant crossover

frequency and proper phase margin are achieved at various working conditions. Therefore, the effectiveness of the proposed control method and system stability are verified. In addition, compared with Fig. 4, the variations of crossover frequency of loop gain and the phase margin in different working conditions are also found to be reduced.

V. Conclusion

Several conclusions have been drawn from the efforts leading to this paper. These are summarized as follows.

1) An AVFPCM control with constant crossover frequency is proposed and experimentally verified for the wide-operation-range USB-PD application.
2) An accurate small-signal model of AVFPCM control is proposed and verified. Based on the model, an adaptive control law is proposed to achieve constant crossover frequency.
3) The proposed control achieves constant crossover frequencies of $G_{\rm vc}(s)$ and loop gain under various working conditions. It eases the compensator design for stability at wide operation range. Moreover, it mitigates the trade-off between stability and transient response. Thus, load transient responses in various conditions are improved. In the experiment, the proposed control reduces the output voltage variation by 43% and 34%, respectively, under 5 and 20 V conditions compared to the traditional VFPCM control. Namely, the proposed control has the advantages of output capacitance reduction and board area reduction in the same load transient specification requirement of the system.

Acknowledgment

The authors would like to thank SIMPLIS Technologies Corporation, U.S.A., for providing the SIMPLIS simulation tool. The authors would also like to thank Tom Yang and other engineers from Richtek Corporation for giving valuable comments.

References

[1] U. S. Padiyar and V. Kamath, "Design and implementation of a universal input flyback converter," in *Proc. IEEE Int. Conf. Elect. Electron. Optim. Techn.*, 2016, pp. 3428–3433.
[2] Y. Li and J. Zheng, "A low-cost adaptive multi-mode digital control solution maximizing AC/DC power supply efficiency," in *Proc. IEEE Appl. Power Electron. Conf.*, 2010, pp. 349–354.
[3] *Highly Integrated Green-Mode PWM Controller: FAN6862 Datasheet*, Fairchild Semiconductor Corporation, 2012. [Online]. Available: http://www.fairchildsemi.com/
[4] *Green-Mode PWM Controller with Latch off Protections: LD7532 Datasheet,* Leadtrend Technology, 2014. [Online]. Available: http://www.leadtrend.com.tw/
[5] *Constant-Voltage Constant-Current Flyback Controller using Opto-Coupled Feedback: UCC28740 Datasheet*, Texas Instruments, 2014. [Online]. Available: http://www.ti.com/
[6] T. T. Vu, S. O'Driscoll, and J. V. Ringwood, "A feasibility study into the robust control of a variable-frequency wide operating range flyback converter," in *Proc. 25th IET Irish Signals Syst. Conf./China-Ireland Int. Conf. Inf. Commun. Technol.*, 2014, pp. 147–152.
[7] L. Huber and M. M. Jovanović, "Small-signal analysis of DCM flyback converter in frequency-foldback mode of operation," in *Proc. 28th Annual IEEE Appl. Power Electron. Conf. Expo.*, 2013, pp. 1746–1752.
[8] B. T. Irving, Y. Panov, and M. M. Jovanović, "Variable-frequency flyback converter," in *Proc. 18th Annual IEEE Appl. Power Electron. Conf. Expo.*, 2003, pp. 977–982.
[9] C. H. Cheng, C. J. Chen, and S. S. Wang, "Small-signal model of flyback converter in continuous-conduction mode with peak-current control at variable switching frequency," *IEEE Trans. Power Electron.*, vol. 33, no. 5, pp. 4145–4156, May 2018.
[10] C. J. Chen, C. H. Cheng, B. S. Wu, and S. S. Wang, "Unified small-signal model and compensator design of flyback converter with peak-current control at variable frequency for USB power delivery," *IEEE Trans. Power Electron.*, to be published, doi: 10.1109/TPEL.2018.2812855.
[11] J. Park *et al.*, "Quasi-resonant (QR) controller with adaptive switching frequency reduction scheme for flyback converter," *IEEE Trans. Ind. Electron.*, vol. 63, no. 6, pp. 3751–3581, Jun. 2016.
[12] Y. C. Kang, C. C. Chiu, M. Lin, C. P. Yeh, J. M. Lin, and K. H. Chen, "Quasi resonant control with a dynamic frequency selector and constant current startup technique for 92% peak efficiency and 85% light-load efficiency flyback converter," *IEEE Trans. Power Electron.*, vol. 29, no. 9, pp. 4959–4969, Sep. 2014.
[13] T. J. Liang, K. H. Chen, and J. F. Chen, "Primary side control for flyback converter operating in DCM and CCM," *IEEE Trans. Power Electron.*, vol. 33, no. 4, pp. 3604–3612, Apr. 2018.
[14] Y. Bai, W. Chen, X. Yang, X. Yang, and J. Sun, "A novel constant current and constant voltage adaptive blanking regulation scheme for primary-side controlled fl nove converter," in *Proc. IEEE 8th Int.. Power Electron. Motion Control Conf*, May 2016, pp. 1652–1659.
[15] Y. T. Lin, T. J. Liang, and K. H. Chen, "IC design of primary-side control for flyback converter," in *Proc. Int. IEEE Future Energy Electron. Conf.*, Nov. 2013, pp. 449–453.
[16] P. Hsieh, C. Chang, and C. Chen, "A primary-side-control quasi-resonant flyback converter with tight output voltage regulation and self-calibrated valley switching," in *Proc. IEEE Energy Convers. Congr. Expo.,* Sep. 2013, pp. 3406–3412.
[17] C. W. Chang and Y. Y. Tzou, "Primary-side sensing error analysis for flyback converters," in *Proc. IEEE 6th Int. Power Electron. Motion Control Conf.*, May 2009, pp. 524–528.
[18] S. Xu, X. Kou, C. Wang, Q. Qian, and W. Sun, "New digital control method for improving dynamic response of synchronous rectified flyback converter with CCM and DCM mode," in *Proc. IEEE Appl. Power Electron. Conf. Expo.*, 2018, pp. 338–343.
[19] C. Wang, S. Xu, and X. Fan, "Novel digital control method for improving dynamic responses of multimode primary-side regulation flyback converter," *IEEE Trans. Power Electron.*, vol. 32, no. 13, pp. 1457–1468, Feb. 2017.
[20] F. He, "USB Port and power delivery: An overview of USB port interoperability," in *Proc. IEEE Symp. Product Compliance Eng.*, 2015, pp. 1–5.
[21] *USB Type-C and USB PD Source Controller: TPS25740 datasheet,* Texas Instruments, 2017. [Online]. Available: http://www.ti.com/
[22] *Application Note AN-4150: Green Current Mode PWM Controller FAN7602,* Fairchild Semiconductor Corporation, 2006. [Online]. Available: http://www.fairchildsemi.com/
[23] *Application Note AN017: Feedback Control Design of Off-line Flyback Converter*, Richtek Technology Corporation, 2014. [Online]. Available: http://www.richtek.com/
[24] R. D. Middlebrook and S. Cuk, "A general unified approach to modeling switching-converter power stages," in *Proc. IEEE Power Electron. Specialists Conf.*, 1976, pp. 18–34.
[25] R. B. Ridley, "A new continuous-time model for current-mode control with constant frequency, constant on-time, and constant off-time, in CCM and DCM," in *Proc. IEEE Power Electron. Specialists Conf.*, 1990, pp. 382–389.
[26] S. Y. Chen, "Small-signal model for a flyback converter with peak current mode control," *IET Power Electron.*, vol. 7, no. 4, pp. 805–810, Apr. 2014.
[27] J. Li and F. C. Lee, "New modeling approach and equivalent circuit representation for current-mode control," *IEEE Trans. Power Electron.*, vol. 25, no. 5, pp. 1218–1230, May 2010.
[28] S. Tian, F. C. Lee, Q. Li, and Y. Yan, "Unified equivalent circuit model and optimal design of V2 controlled buck converters," *IEEE Trans. Power Electron.*, vol. 31, no. 2, pp. 1734–1744, Feb. 2016.
[29] Y. Yan, F. Lee, P. Mattavelli, and P. H. Liu, "Average current mode control for switching converters," *IEEE Trans. Power Electron.*, vol. 29, no. 4, pp. 2027–2036, Apr. 2014.

[30] S. F. Hsiao, D. Chen, C. J. Chen, and H. S. Nien, "A new multiple-frequency small-signal model for high-bandwidth computer v-core regulator applications," *IEEE Trans. Power Electron.*, vol. 29, no. 4, pp. 2027–2036, Apr. 2014.
[31] Y.-C. Lin, C.-J. Chen, D. Chen, and B. Wang, "A ripple-based constant on-time control with virtual inductor current and offset cancellation for dc power converters," *IEEE Trans. Power Electron.*, vol. 27, no. 10, pp. 4301–4310, Oct. 2012.
[32] C. H. Cheng, C. J. Chen, and S. S. Wang, "An overview of stability improvement method for wide-operation-range flyback converter with variable frequency peak-current-mode control," in *Proc. Int. Power Electron. Conf.*, May 2018.

Ching-Hsiang Cheng (S'18) was born in Chiayi, Taiwan, R.O.C. He received the B.S. degree in electrical engineering from the National Yunlin University of Science and Technology, Yunlin, Taiwan, in 2010 and the M.S. degree in electrical engineering from National Tsing Hua University, Hsinchu, Taiwan, in 2012. He is currently working toward the Ph.D. degree at the Electrical Engineering Department, National Taiwan University, Taipei.

Since 2012, he has been working as an Engineer in the System Development Center with Richtek Technology Corporation, Hsinchu, Taiwan, where his work focuses on system analysis and design of controller for ac–dc charger. His research interests include modeling, analysis, and control of ac–dc and dc–dc power converters, power integrated circuits, smart power management integrated circuits, and thermal evaluation for monolithic power integrated circuits.

Ching-Jan Chen (S'08–M'12–SM'18) received the B.S. and Ph.D. degrees in electrical engineering from National Taiwan University, Taipei, Taiwan, in 2006 and 2011, respectively.

From 2010 to 2011, he was a Visiting Scholar with the Center of Power Electronic Systems (CPES) of Virginia Tech., Blacksburg. From 2011 to 2015, he was a Senior Engineer with IC Research and Development Department at Richtek Technology Corporation, Hsinchu, Taiwan. Since 2015, he has been working as an Assistant Professor with the Department of Electrical Engineering, National Taiwan University, Taiwan. His research interests include modeling and control of dc–dc and ac–dc power converters, power conversion for CPU and mobile devices, and power IC design.

Shinn-Shyong Wang received the bachelor's and doctoral degrees in electrical engineering from Tsinghua University, Hsinchu, Taiwan, in 1981 and 1989, respectively.

Since 2011, he has been with Richtek Technology Corp., formerly as VP of System Development Center and presently as a Technical Consultant. His research interests include switching converter analysis, design, and related technology development.